Effects of Changes in Chemistry and Testing Temperature on Mechanical Behavior of Al-Based Amorphous Alloy Ribbons

CHUN-KUO HUANG and JOHN J. LEWANDOWSKI

The effects of changes in composition, testing temperature, strain rate, and thermal exposure on the flow behavior of a series of Al-Gd-Ni-X amorphous alloy ribbons have been determined via hot microhardness and tension testing. It is shown that the addition of Fe, Co, and Fe/Co combination into these materials increases the strength, T_g, and T_{x1} in addition to the activation energy for crystallization, whereas the window between T_g and T_{x1} remains similar. The uniaxial tensile tests show these ribbons exhibit a high strength, around 1 GPa, at room temperature (RT), and the results also show that these ribbons maintain their strength, nearly 45 pct of their RT value, at temperatures near T_g. Scanning electron microscopy images of fracture surfaces obtained from tests conducted near T_g illustrate ductile rupture and homogeneous flow behavior near the fracture tip.

DOI: 10.1007/s11661-010-0303-6

I. INTRODUCTION

A combination of good strength and low density (*i.e.*, specific strength) is necessary for structural materials. Significant interest has developed in amorphous and nanocrystalline aluminum alloys in recent years because of their high strength and low density.[1] The most important group of Al-based amorphous alloys are the aluminum-rare earth-transition metal (Al-RE-TM) system alloys because of their good glass-forming ability and mechanical properties.[2–4] These alloys have been shown to exhibit strengths almost twice that of conventional Al alloys (7075-T6: $\sigma_y \approx 500$ MPa) with similar densities as conventional Al alloys.[1]

Recent research has been investigating the effects of annealing on devitrification and the subsequent mechanical properties of an Al-Gd-Ni alloy.[3,5–7] The results showed that $Al_{87}Gd_6Ni_7$ exhibited a low-onset crystallization temperature T_{x1}, 462 K (189 °C), and tensile tests showed that the precipitation of pure α-Al nano particles from the glassy matrix, thereby enriching the local matrix in Gd and Ni, produced embrittlement. In the past decade, many efforts have investigated the effects of compositional changes on the thermal stability of amorphous alloys.[2,8–10] It has been shown that an increase in the amount of transition metal elements has a significant effect on T_x for Al-RE-TM amorphous alloys.[2] In this study, the effects of Fe and Co additions in an Al-Gd-Ni amorphous alloy ($Al_{87}Gd_6Ni_7$) are represented. The flow and fracture behavior across a range of testing temperatures and strain rates is characterized.

CHUN-KUO HUANG, Graduate Student, and JOHN J. LEWANDOWSKI, Leonard Case Professor of Engineering, are with the Department of Materials Science and Engineering, Case Western Reserve University, Cleveland, OH 44106, USA. Contact e-mail: jjl3@case.edu

Manuscript submitted November 24, 2009.
Article published online May 25, 2010

II. EXPERIMENTAL PROCEDURES

The materials ($Al_{86}Gd_6Ni_7Fe_1$, $Al_{86}Gd_6Ni_7Co_1$, $Al_{85}Gd_6Ni_7Fe_2$, and $Al_{85}Gd_6Ni_7Fe_1Co_1$) were produced by Ames Laboratory (Ames, IA) via the melt spinning technique using a rotating chilled copper block at a wheel speed of 16 m/s. The melt spinning process was in a well-controlled He atmosphere of 0.3 atm. The as-received ribbons have a thickness of 50 μm and a width of 1.8 mm. The ribbons were confirmed amorphous by X-ray diffraction (XRD; X1; Scintag, Cupertino, CA) using Cu Kα radiation with a scan rate of 3 deg/min on the air side of the ribbons in addition to transmission electron microscopy (TEM) described subsequently. Thermal stability analysis was performed by differential scanning calorimetry (DSC; DSC822^e; Mettler Toledo, Aurora, IL) with a heating rate of 3 K/min (3 °C/min)—identical to the heating rate used in the high-temperature tensile tests. Young's modulus was measured via the nanoindentation technique (Hysitron Triboscope, Minneapolis, MN) using a load of 2000 *u*N and a loading rate of 1×10^{-4} N/s. A Nikon QM hot microhardness tester (Nikon Instruments, Melville, NY) with a diamond Vickers indenter was used to determine the hardness evolution during heating. The specimen and indenter were heated separately at a heating rate of 10 K/min (10 °C/min), and the hardness was measured on the air side of the ribbon at 298 K (25 °C), 373 K (100 °C), 423 K (150 °C), 448 K (175 °C), 473 K (200 °C), and 498 K (225 °C). Some samples were tested additionally at 523 K (250 °C) and 548 K (275 °C). To investigate the evolution of hardness at a fixed high temperature, separate studies were performed on as-received ribbons. In these cases, the specimen and indenter were heated directly to 498 K (225 °C) at a rate of 10 K/min (10 °C/min), and the hardness was measured at a variety of holding times at 498 K (225 °C). All indents were performed using a load of 100 *g* and a loading time of 15 seconds.[11] The annealed ribbons were investigated

further by XRD and TEM. TEM analyses on ribbons annealed at 498 K (225 °C) were conducted by FEI Tecnai F30 (FEI, Hillsboro, OR). The TEM specimens were prepared by electropolishing at 243 K (−30 °C) in a solution 30 pct nitric acid and 70 pct methanol. Tensile tests were performed with an Instron tabletop tester model 1026 (Instron, Norwood, MA) and were carried out under room temperature (RT), 373 K (100 °C), and 473 K (200 °C) with a heating rate of 3 K/min (3 °C/min), and a strain rate ranging from 1×10^{-3}/s to 5×10^{-4}/s. Tensile specimens were ground carefully using grit polishing into an hour-glass shape with a gauge length of 10 mm, a width of 1 mm, and a thickness of 50 *u*m. This was conducted to remove the nonuniform edges typically present on melt spun ribbon samples. The curvature of the reduced section was 28 mm, and the corresponding stress concentration factor k_t was close to 1.0. The fracture surfaces were examined by scanning electron microscopy (SEM).

III. RESULTS

The XRD traces for as-received ribbons are shown in Figure 1(a). The lack of long-range crystallinity is confirmed by the presence of a broad and diffuse peak and is a typical characteristic of amorphous materials. DSC conducted on as-received Al-based amorphous alloy ribbons at a heating rate of 3 K/min (3 °C/min) reveals the effect of adding Fe/Co on the onset of T_g, as shown in Figure 2. The onset of T_g and T_{x1} was determined according to ASTM E537-02 and ASTM E1356-03. Compared with the $Al_{87}Gd_6Ni_7$ alloy, the onset of T_{x1} is delayed 30 K (30 °C) by a substitution of 1-at pct Fe/Co for Al, and the onset of T_{x1} is further increased by an addition of 2-at pct constituents.[5] However, the gap between T_g and T_{x1} does not show a noticeable increase with an addition of 1-at pct Fe/Co, and it reduces roughly 5 K (5 °C) in $Al_{85}Gd_6Ni_7Fe_2$ and $Al_{85}Gd_6Ni_7Fe_1Co_1$ ribbons.

The DSC results on the location of T_g and T_{x1} are confirmed further by high-temperature microhardness tests. Figure 3(a) shows the effect of an addition of Fe/Co and changes in testing temperature on microhardness. A significant softening was observed at testing temperatures around T_g for all ribbons. When the microhardness testing temperature passed T_{x1}, noticeable hardening occurred because of crystallization. The effects of holding at a fixed temperature around T_{x1} on the evolution of

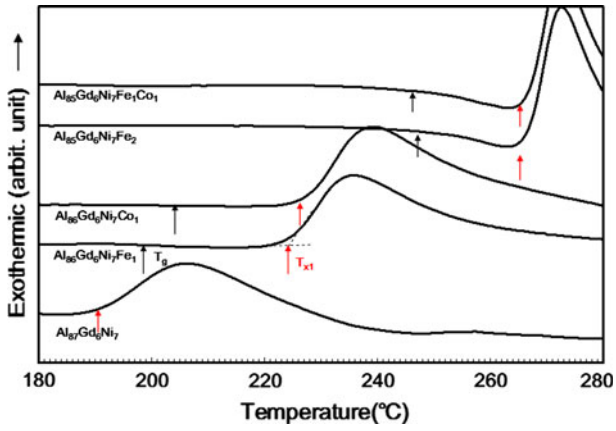

Fig. 2—DSC traces of as-received $Al_{87}Gd_6Ni_7$, $Al_{86}Gd_6Ni_7Fe_1$, $Al_{86}Gd_6Ni_7Co_1$, $Al_{85}Gd_6Ni_7Fe_2$, and $Al_{85}Gd_6Ni_7Fe_1Co_1$ ribbons measured at a heating rate of 3 K/min (3 °C/min). T_g and T_{x1} are denoted by arrows.

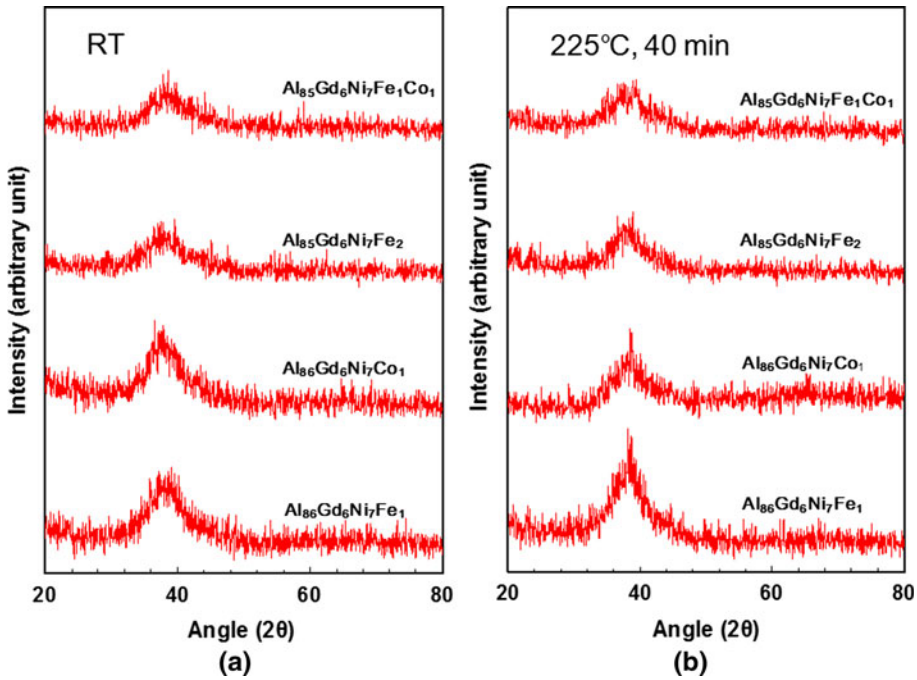

Fig. 1—XRD traces of $Al_{86}Gd_6Ni_7Fe_1$, $Al_{86}Gd_6Ni_7Co_1$, $Al_{85}Gd_6Ni_7Fe_2$, and $Al_{85}Gd_6Ni_7Fe_1Co_1$ ribbons. (*a*) As-received ribbons. (*b*) Annealed at 498 K (225 °C) for 40 min.

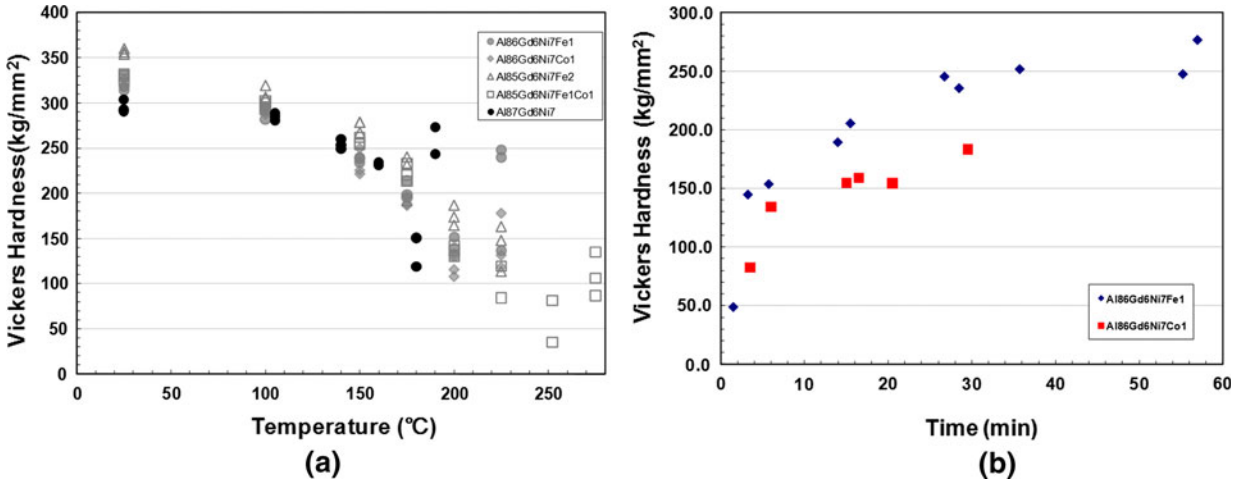

Fig. 3—Vickers microhardness evolution of $Al_{87}Gd_6Ni_7$, $Al_{86}Gd_6Ni_7Fe_1$, $Al_{86}Gd_6Ni_7Co_1$, $Al_{85}Gd_6Ni_7Fe_2$, and $Al_{85}Gd_6Ni_7Fe_1Co_1$ ribbons. (*a*) Effects of changes in testing temperature. (*b*) Effects of exposure time at a fixed temperature (*i.e.*, 498 K (225 °C)).

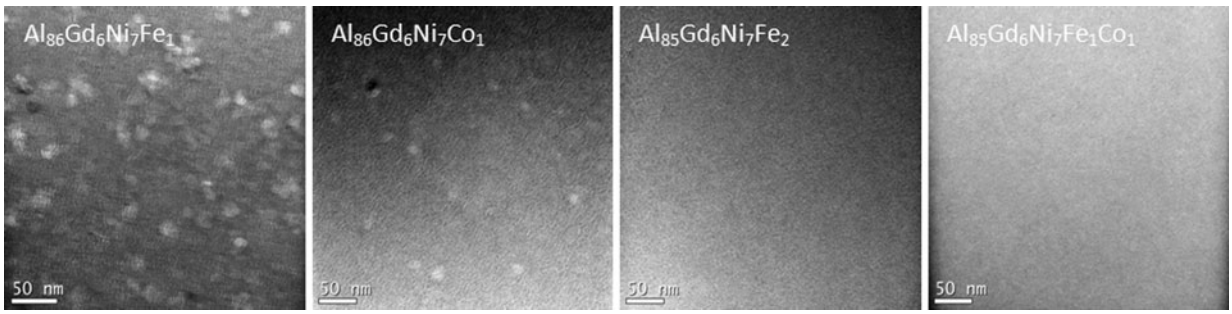

Fig. 4—TEM bright field images of $Al_{86}Gd_6Ni_7Fe_1$, $Al_{86}Gd_6Ni_7Co_1$, $Al_{85}Gd_6Ni_7Fe_2$, and $Al_{85}Gd_6Ni_7Fe_1Co_1$ ribbons annealed at 498 K (225 °C) for 40 min.

microhardness were evaluated on separate $Al_{86}Gd_6Ni_7Fe_1$ and $Al_{86}Gd_6Ni_7Co_1$ ribbons. Figure 3(b) shows that the hardness of $Al_{86}Gd_6Ni_7Fe_1$ and $Al_{86}Gd_6Ni_7Co_1$ ribbons increased significantly in the first 10 minutes exposed to 498 K (225 °C) and reached a steady state after 30 minutes and 15 minutes, respectively. These results also reveal that the first crystallization temperature for $Al_{86}Gd_6Ni_7Fe_1$ and $Al_{86}Gd_6Ni_7Co_1$ alloys is around 498 K (225 °C) and that it may take 15 to 30 minutes at this temperature for the first crystallization process to develop fully. XRD and TEM analyses confirm the amorphous nature of the as-spun ribbons and the formation of α-Al after isothermal annealing at 498 K (225 °C) for 40 minutes. Figure 1(b) shows that $Al_{86}Gd_6Ni_7Fe_1$ and $Al_{86}Gd_6Ni_7Co_1$ ribbons exhibit a sharpened peak located at an angle (2θ) of 38.5 deg, which corresponds to the X-ray beam reflection from (111) plane of α-Al. The volume fraction of the crystalline phase was determined from the integrated areas of amorphous and crystalline peaks according to the following[12]:

$$V_f = \frac{A_{cryst}}{A_{cryst} + A_{amor}}$$

where V_f is the volume fraction of crystalline α-Al formed from fully amorphous matrix, A_{cryst} is the integrated area corresponding to crystalline peaks, and A_{amor} is the total area corresponding to an amorphous peak. The volume fractions of crystalline α-Al phase are 9.5 pct and 6.0 pct for $Al_{86}Gd_6Ni_7Fe_1$ and $Al_{86}Gd_6Ni_7Co_1$ after annealing, respectively. The TEM bright field images provided in Figure 4 show some α-Al nanoparticles in $Al_{86}Gd_6Ni_7Fe_1$ and $Al_{86}Gd_6Ni_7Co_1$ ribbons after annealing. The volume fraction of α-Al particles in $Al_{86}Gd_6Ni_7Fe_1$ is much higher than that in the $Al_{86}Gd_6Ni_7Co_1$ ribbon. However, crystallization of α-Al did not occur in $Al_{85}Gd_6Ni_7Fe_2$ and $Al_{85}Gd_6Ni_7Fe_1Co_1$ ribbons for the same exposure conditions as shown in Figure 1(b) and Figure 4.

Mechanical properties of $Al_{86}Gd_6Ni_7Fe_1$, $Al_{86}Gd_6Ni_7Co_1$, $Al_{85}Gd_6Ni_7Fe_2$, and $Al_{85}Gd_6Ni_7Fe_1Co_1$ ribbons are summarized in Table I. Figure 5 shows the engineering stress–strain curves of $Al_{86}Gd_6Ni_7Co_1$ ribbons tested in tension at RT, 373 K (100 °C), and 473 K (200 °C) as a typical example for these kinds of materials. Note that the global strain to failure for these specimens is not accurate because these tensile specimens are too small to apply a strain gauge. All tensile specimens failed via catastrophic shear at a strain rate of 10^{-3} seconds^{-1} at RT and 373 K (100 °C), and they displayed no macroscopic deformation prior to failure. The fracture strength for all four materials ranges from 850 MPa to 1050 MPa at RT, and it drops slightly to 90 pct of its original value at 373 K

Table I. Mechanical Properties of $Al_{86}Gd_6Ni_7Fe_1$, $Al_{86}Gd_6Ni_7Co_1$, $Al_{85}Gd_6Ni_7Fe_2$, and $Al_{85}Gd_6Ni_7Fe_1Co_1$ Ribbons at RT*

Alloy (At Pct)	σ_f (MPa)	E (GPa)	$\varepsilon_{c,f}$ (Pct)	ρ_c (g/cm^3)	$\sigma_{f/\rho}$ (10^5 Nm/kg)	Hv (kg/mm^2)	$\sigma_{c,y}$ (MPa)	T_g (K (°C))	T_{x1} (K (°C))
$Al_{86}Gd_6Ni_7Fe_1$	1055	82.1	1.3	3.61	2.92	320	1050	471 (198)	497 (224)
$Al_{86}Gd_6Ni_7Co_1$	1075	85.1	1.3	3.62	2.97	325	1065	477 (204)	501 (228)
$Al_{85}Gd_6Ni_7Fe_2$	850	88.6	1.0	3.65	2.33	355	1160	523 (250)	539 (266)
$Al_{85}Gd_6Ni_7Fe_1Co_1$	950	89.8	1.0	3.66	2.60	330	1075	522 (249)	539 (266)
$Al_{87}Gd_6Ni_7$	880	71.3	1.2	3.58	2.46	300	970	441 (168)	462 (189)

*σ_f = tensile fracture strength; E = Young's modulus; $\varepsilon_{c,f}$ = calculated fracture strain; ρ_c = calculated density; Hv = Vickers hardness number; $\sigma_{c,y}$ = calculated compressive yield strength.

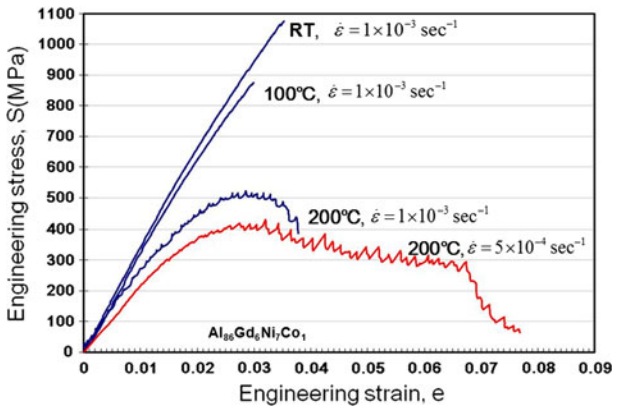

Fig. 5—Engineering stress–strain curves of $Al_{86}Gd_6Ni_7Co_1$ ribbons tested at RT, 373 K (100 °C), and 473 K (200 °C) at 1×10^{-3}/s and at 473 K (200 °C) at 5×10^{-4}/s.

(100 °C). All tensile results obtained the same order of strength as that estimated from hot hardness test results as shown in Table I.

The fracture surface of $Al_{86}Gd_6Ni_7Co_1$ ribbon tested at 373 K (100 °C) is shown in Figure 6(a). Typical features for locally ductile metallic glass are presented, such as well-developed vein patterns, although the macroscopic ductility is zero and the fracture is via shear.

From the stress–strain curves in Figure 5, the flow behavior shows a significant difference between 1×10^{-3} seconds^{-1} and 5×10^{-4} seconds^{-1} for $Al_{86}Gd_6Ni_7Co_1$ at 473 K (200 °C). The elongation to failure almost doubled at a slower strain rate of 5×10^{-4} seconds^{-1}, and the peak stress also dropped about 20 pct compared with the test conducted at a strain rate of 1×10^{-3} seconds^{-1}. Figure 6(b) shows the fracture surface for the $Al_{86}Gd_6Ni_7Co_1$ sample subjected to a tensile test at 473 K (200 °C) at a strain rate of 5×10^{-4} seconds^{-1}. The ductile rupture was revealed, and the alloy showed homogeneous plasticity near the fracture tip, resulting in a viscous-like feature with a reduction in area of more than 90 pct as shown in the inset of Figure 6(b). Although more homogeneous deformation was achieved near T_g under slow strain rate conditions, this material still exhibited a remarkably high stress—45 pct of its strength at RT. Tests conducted at a higher strain rate of 1×10^{-3} seconds^{-1} at 473 K (200 °C) produced a transition from ductile rupture to vein patterns, representing a

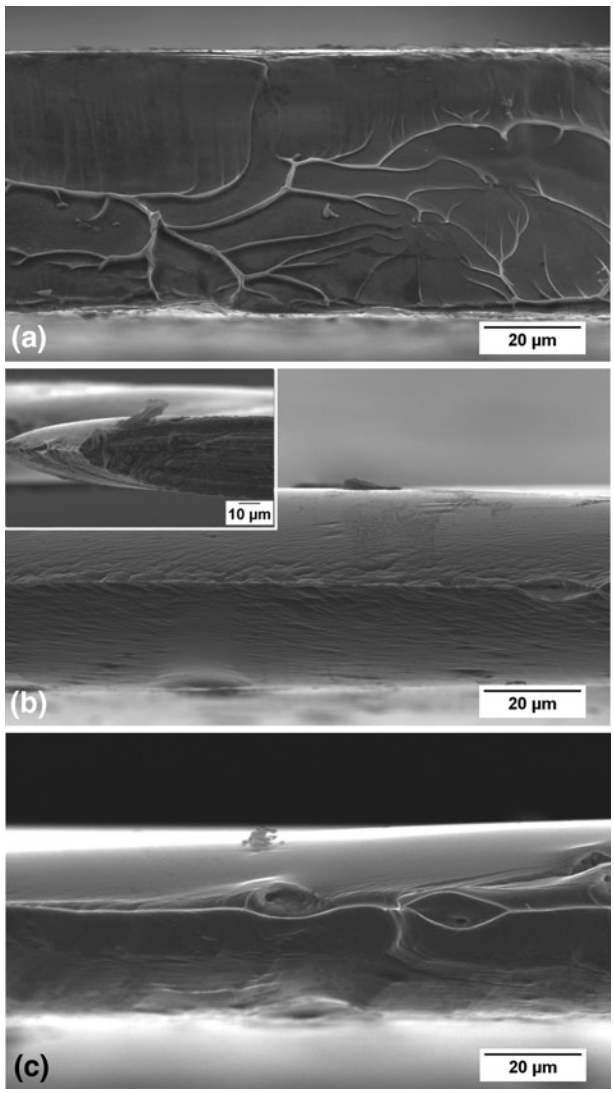

Fig. 6—Fracture surfaces of ribbons tested at various conditions. (*a*) $Al_{86}Gd_6Ni_7Co_1$ ribbon tested at 373 K (100 °C) and 1×10^{-3}/s. (*b*) $Al_{86}Gd_6Ni_7Co_1$ ribbon tested at 473 K (200 °C) and 5×10^{-4}/s. (*c*) $Al_{85}Gd_6Ni_7Fe_1Co_1$ ribbon tested at 473 K (200 °C) and 5×10^{-4}/s.

transition from homogeneous flow to more inhomogeneous flow. Similar behavior also was exhibited by the $Al_{85}Gd_6Ni_7Fe_2$ and $Al_{85}Gd_6Ni_7Fe_1Co_1$ ribbons, as shown in Figure 6(c). Table II summarizes the tensile observations on the other systems examined.

Table II. Summary of Tensile Properties Tested at RT, 373 K (100 °C), and 473 K (200 °C)

Alloy (At Pct)	T/T_g	$\dot{\varepsilon}$ (s^{-1})	UTS (MPa)	Reduction in Area	Fracture Mode	Flow Behavior
$Al_{86}Gd_6Ni_7Fe_1$	0.633	1×10^{-3}	1055	<1.0 pct	Shear	Serrated
	0.792	1×10^{-3}	900	<1.0 pct	Shear	Serrated
	1.004	5×10^{-4}	375	90.0 pct	Ductile rupture	Smooth
$Al_{86}Gd_6Ni_7Co_1$	0.625	1×10^{-3}	1075	<1.0 pct	Shear	Serrated
	0.782	1×10^{-3}	870	<1.0 pct	Shear	Serrated
	0.992	1×10^{-3}	515	53.0 pct	Shear/ductile rupture	Serrated
	0.992	5×10^{-4}	430	93 pct	Ductile rupture	Smooth
$Al_{85}Gd_6Ni_7Fe_2$	0.570	1×10^{-3}	850	<1.0 pct	Shear	Serrated
	0.713	1×10^{-3}	830	<1.0 pct	Shear	Serrated
	0.904	5×10^{-4}	660	54.0 pct	Shear/ductile rupture	Serrated
$Al_{85}Gd_6Ni_7Fe_1Co_1$	0.570	1×10^{-3}	950	<1.0 pct	Shear	Serrated
	0.714	1×10^{-3}	920	<1.0 pct	Shear	Serrated
	0.906	5×10^{-4}	610	52.0 pct	Shear/ductile rupture	Serrated

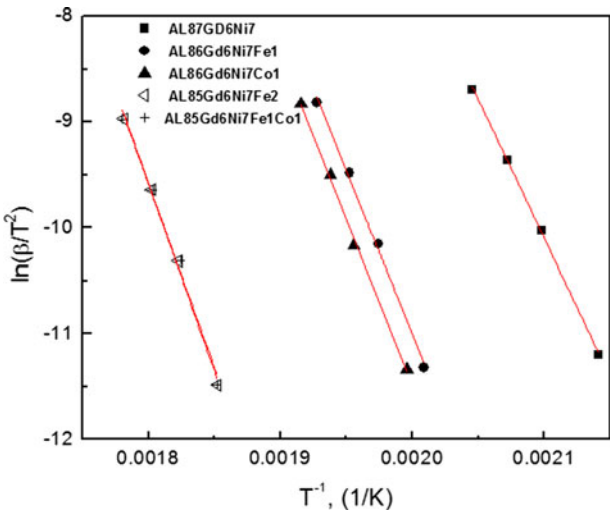

Fig. 7—ln (β/T^2) *vs* 1/T plot for all ribbons tested at different heating rates. The slope is used to estimate the activation energy for crystallization according to Kissinger's method.[14]

IV. DISCUSSION

It is observed that the addition of Fe/Co to $Al_{87}Gd_6Ni_7$ has a significant effect on the position of T_g and $T_{\times 1}$. Because T_g and T_{x1} increase significantly with an increasing Fe/Co concentration, it suggests that the interatomic bonding between Al-Fe or between Al-Co is stronger than Al-Al bonding. The predicted values for the interfacial enthalpy of Fe solved in Al $\left(\Delta H^{\text{int}}_{\text{Fe in Al}}\right)$ and Co solved in Al $\left(\Delta H^{\text{int}}_{\text{Co in Al}}\right)$ are −79 kJ/mol and −105 kJ/mol, respectively.[13] Therefore, the Co addition should increase T_g and T_{x1} to higher temperatures than the Fe addition. However, our DSC result only showed little difference. To estimate the changes in activation energy for crystallization as a result of these chemistry changes, additional DSC traces were conducted at heating rates of 10 K/min (10 °C/min), 20 K/min (20 °C/min), and 40 K/min (40 °C/min). By following Kissinger's method, the effects of such changes on the heating rate are summarized in Figure 7, and the activation energy for crystallization E_a can be derived from the slope in the figure according to the following equation[14]:

$$\ln\left(\frac{\beta}{T^2}\right) = -\frac{E_a}{RT} + C$$

where β is the heating rate and E_a is the activation energy for crystallization. E_a also is summarized in Table III. The addition of Fe/Co clearly increases E_a from 218 KJ/mol to 289 KJ/mol, depending on the amount of solute added, and the amorphous ribbons become more stable.

High-temperature microhardness test results show softening at 423 K (150 °C) (0.85 to 0.9 T_g) because the glassy structure starts to relax. The microhardness is lowest at 473 K (200 °C) (near T_g) for $Al_{86}Gd_6Ni_7Fe_1$ and $Al_{86}Gd_6Ni_7Co_1$ ribbons, but it increases at 498 K (225 °C) (near T_{x1}) as a result of crystallization. One potential source of such strengthening relates to the precipitation of α-Al nanocrystals because these particles could act as barriers and hinder the matrix flow at higher temperatures.[11,15] However, the formation of α-Al nanocrystals also requires chemical redistribution in the matrix. The solute-enriched glassy matrix caused by precipitation of pure α-Al particles also may result in an increase in microhardness. The changes in solute concentration after annealing were estimated from the volume fraction of α-Al obtained according to XRD analysis in the manner previously used by Wesseling *et al.*[16] as shown in Figure 8, assuming the rejected solute is distributed homogeneously in the amorphous matrix. The results show that the microhardness depends linearly on the solute concentration in the matrix, suggesting that the enrichment of solute is more likely the main strengthening mechanism, as proposed in previous reports,[16,17] and is consistent with the effects of the chemistry changes on the hardness changes in the amorphous ribbons, also shown in Figure 8.

Tensile tests performed at RT and at 373 K (100 °C) show that the fracture surfaces are produced by shear with microscopic vein patterns typical of locally ductile flow. The fracture tip reveals an angle around 55 deg with respect to the tensile stress direction. Tensile tests performed at 473 K (200 °C) demonstrate mechanical behavior consistent with the behavior of metallic glasses deformed in the homogeneous flow regime, as reported earlier,[18–22] with a significant strain rate dependence.

Table III. T_g, T_{x1}, and Activation Energy for Crystallization Estimated from DSC Traces According to Kissinger's Method

Alloy (At Pct)	$Al_{86}Gd_6Ni_7Fe_1$	$Al_{86}Gd_6Ni_7Co_1$	$Al_{85}Gd_6Ni_7Fe_2$	$Al_{85}Gd_6Ni_7Fe_1Co_1$	$Al_{87}Gd_6Ni_7$
T_g (K (°C))	471 (198)	477 (204)	523 (250)	522 (249)	441 (168)
T_{x1} (K (°C))	497 (224)	501 (228)	539 (266)	539 (266)	462 (189)
E_a (kJ/mol)	253	262	288	289	218

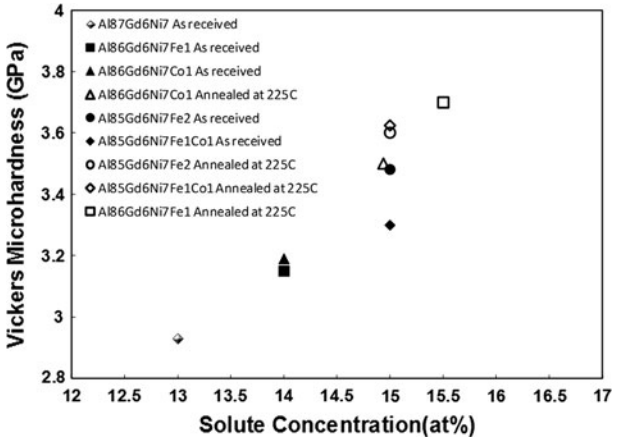

Fig. 8—Vickers microhardness *vs* solute concentration from as-received chemistry or XRD for annealed ribbons.

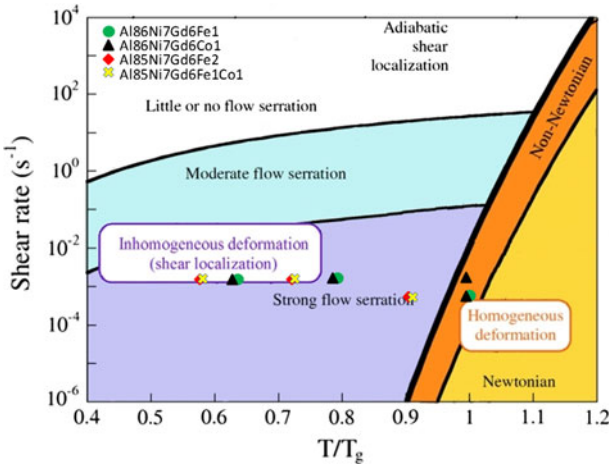

Fig. 9—Present tension results plotted on a deformation map. Non-Newtonian homogeneous deformation was captured at $T/T_g \sim 1$ and at a slow strain rate. All other test conditions produced inhomogeneous deformation as indicated by the SEM images of fracture surfaces.

The significant increase of strain to failure and the reduction in area indicate characteristics of homogeneous deformation as the strain rate decreases to 5×10^{-4} seconds^{-1}. The stress overshoot phenomena captured is consistent with nonsteady-state homogeneous flow behavior that develops because the structural relaxation is not fast enough to accommodate the strain rate. The present work also shows that the transition of flow behavior from inhomogeneous to more homogeneous depends not only on strain rate but also on slight changes in chemical composition because the T_g of $Al_{85}Gd_6Ni_7Fe_2$ and $Al_{85}Gd_6Ni_7Fe_1Co_1$ further increase to ~498 K (225 °C). The testing conditions used in the present work and summarized in Table II are superimposed on Schuh's deformation map as shown in Figure 9.[23,24] The predicted flow behavior is consistent with the present test results. Homogeneous deformation is observed at $T/T_g \sim 1$ and at a strain rate lower than 1×10^{-3} seconds^{-1} as indicated by SEM images of fracture surfaces.

V. SUMMARY

The effects of Fe/Co additions on the thermal stability and mechanical behavior of Al-Gd-Ni amorphous ribbons have been investigated. DSC, XRD, TEM, and high-temperature hardness results show that T_g and T_{x1} increase significantly because of the stronger bonding between Al-Fe/Co compared with Al-Al. The activation energy for crystallization has been quantified, and it increases with an increase in Fe and/or Co, which stabilizes these materials in comparison with the base Al-Gd-Ni alloy at temperatures lower than T_{x1}. Microhardness testing after annealing revealed strengthening that was attributed to solute enrichment in the amorphous matrix and caused by the formation of α-Al nano-particles, which is also consistent with the effects of chemistry changes in the hardness/strength of the amorphous ribbons. A transition from an inhomogeneous flow to a more homogeneous flow was obtained at low strain rates upon approaching T_g, whereas the deformation behavior at different strain rates and temperatures was captured in a deformation map.

ACKNOWLEDGMENTS

The authors thank the DARPA-SAM 2 program for support through Pratt & Whitney Corporation. Supply of materials from Pratt & Whitney and Ames Laboratory is gratefully acknowledged. Useful discussions with A. L. Greer and G. J. Shiflet along with TEM conducted by Dinqiang Li are also appreciated.

REFERENCES

1. A.L. Greer: *Science*, 1995, vol. 267, p. 1947.
2. A. Inoue, K. Ohtera, A.P. Tsai, and T. Masumoto: *Jpn. J. Appl. Phys.*, 1988, vol. 27, p. L280.
3. Y. He, S.J. Poon, and G.J. Shiflet: *Science*, 1988, vol. 241, p. 1640.
4. A. Inoue, S. Sobu, D.V. Louzguine, H. Kimura, and K. Sasamori: *J. Mater. Res.*, 2004, vol. 19, p. 1539.
5. B.C. Ko, P. Wesseling, O.L. Vatamanu, G.J. Shiflet, and J.J. Lewandowski: *Intermetallics*, 2002, vol. 10, p. 1099.

6. M.C. Gao and G.J. Shiflet: *Intermetallics*, 2002, vol. 10, p. 1131.
7. P. Wesseling, B.C. Ko, and J.J. Lewandowski: *Scripta Mater*., 2003, vol. 48, p. 1537.
8. A. Inoue: *Progr. Mater. Sci*., 1998, vol. 43, p. 365.
9. A. Zhu, S.J. Poon, and G.J. Shiflet: *Scripta Mater*., 2004, vol. 50, p. 1451.
10. H.W. Yang, S.C. Tjong, and J.Q. Wang: *Mater. Sci. Eng*., 2005, vol. 406, p. 160.
11. A.S. Nouri, Y. Liu, and J.J. Lewandowski: *Metall. Mater. Trans. A*, 2009, vol. 40A, p. 1314.
12. T. Gloriant, M. Gich, S. Surnach, M.D. Baro, and A.L. Greer: *J. Metastable Nanocryst. Mater*., 2000, vol. 8, p. 365.
13. H. Bakker: *Enthalpies in Alloys: Miedema's Semi-Empirical Model*, Trans Tech Publications Inc., Zurich, Switzerland, 1998.
14. H.E. Kissinger: *Anal. Chem*., 1957, vol. 29, p. 1702.
15. R. Yavari, J.J. Lewandowski, and J. Eckert: *MRS Bulletin*, 2007, vol. 32, p. 635.
16. P. Wesseling, B.C. Ko, L.O. Vatamani, G.J. Shiflet, and J.J. Lewandowski: *Metall. Mater. Trans. A*, 2008, vol. 39A, p. 1935.
17. Z.C. Zhong, X.Y. Jiang, and A.L. Greer: *Mater. Sci. Eng. A*, 1997, vols. 226–228, p. 531.
18. T.G. Nieh, J. Wadsworth, C.T. Liu, T. Ohkubo, and Y. Hirotsu: *Acta Mater*., 2001, vol. 49, p. 2887.
19. J. Lu, G. Ravichandran, and W.L. Johnson: *Acta Mater*., 2003, vol. 51, p. 3429.
20. M. Bletry, P. Guyot, Y. Brechet, J.J. Blandin, and J.L. Soubeyroux: *Intermetallics*, 2004, vol. 12, p. 1051.
21. T.G. Nieh and J. Wadsworth: *Scripta Mater*., 2006, vol. 54, p. 387.
22. A.H. Vormelker, O.L. Vatamanu, L. Kecskes, and J.J. Lewandowski: *Metall. Mater. Trans. A*, 2008, vol. 39A, p. 1922.
23. C.A. Schuh, A.C. Lund, and T.G. Nieh: *Acta Mater*., 2004, vol. 52, p. 5879.
24. L.A. Deibler and J.J. Lewandowski: *Mater. Sci. Eng. A*, 2010, vol. 527, p. 2214.